Letter

# Bulk Probing of Shock Wave Spatial Distribution in Opaque Solids by Ultrasonic Interaction

M. Ducousso,[1,*] E. Cuenca,[1,2,3] M. Marmonier,[1] L. Videau,[4,5] F. Coulouvrat,[3] and L. Berthe[2]

[1] *Safran Tech, Rue des jeunes Bois, 78114 Magny les Hameaux, France*

[2] *Laboratoire Procédés et Ingénieries en Mécanique et Matériaux, CNRS, Arts et Métiers Paris Tech, 151 Boulevard de l'Hôpital, 75013 Paris, France*

[3] *Sorbonne Université, Institut Jean Le Rond d'Alembert, UMR CNRS 7190, 4 place Jussieu, 75005 Paris, France*

[4] *CEA, DAM, DIF, F-91297 Arpajon, France*

[5] *Université Paris-Saclay, CEA, Laboratoire Matière en Conditions Extrêmes, 91680 Bruyéres-le-Châtel, France*

(Received 11 December 2020; revised 5 March 2021; accepted 16 April 2021; published 20 May 2021)

We present a method to investigate the bulk propagation of a shock wave in a thick, opaque metallic plate. The shock wave is generated by laser loading. An elastic plane probe wave, counter-propagative with respect to the shock, is emitted by means of a phase-array device. Shock propagation monitoring is performed by analyzing on the phase-array detection the acoustic elastic plane wave after its interaction with the shock. The time-space detection of the probe wave allows the evaluation of the spatial distribution of the shock wave all along its propagation in the opaque structure, from near to far field. Applications range from fundamental wave science to laser-loading material science.

DOI: 10.1103/PhysRevApplied.15.L051002

## I. INTRODUCTION

Longitudinal shock wave propagation in opaque materials can be imaged only using large high-brilliance X-ray facilities [1,2]. Elastography, proposed by Ophir *et al.* [3], is an acoustic based technique developed to image the shear elasticity of biological tissues by mapping bulk elastic properties of materials through ultrasound (US). The general principle is to generate a relatively low-frequency shear modulation, while a high-frame-rate longitudinal probe wave records the response to this modulation [4,5]. Magnetic resonance imaging can also be used instead of US [6]. Elastography has already been used to monitor shear shock waves [7], even inside the brain [8–10]. However, such an imaging technique cannot be used to image laser-driven shock propagation in hard materials, as it requires a large ratio between longitudinal and shear wave velocities, of the order of $10^3$.

At the laboratory scale, except for certain classes of soft materials and also transparent ones, only shock-induced surface displacement or velocities can be monitored, using optical [11] or piezoelement setups [12]. However, imaging at the laboratory scale could efficiently bring new understandings into shock wave physics, such as caustic formation or Mach reflection in solids, into warm dense matter, for high pressure and temperature phase diagram exploration, [13] or into engineering applications of shock waves. [14,15].

Burgers [16] and Brillouin [17] introduced a pioneering model of the nonlinear interaction between an acoustic wave and a high-amplitude shock in fluids. A detailed analysis of all possible waves (acoustic, entropy, or vorticity ones) diverging from a shock, and of the distortion of the shock itself, was achieved by McKenzie and Westphal [18]. This theory has found multiple applications in aerodynamics [19], aeroacoustics [20], and magnetohydrodynamics [21,22]. Most of these applications involve strong shocks, with Mach numbers much above unity. Regarding a solid medium, very few theoretical papers exist [23].

The objective of this paper is to demonstrate the possibility of using this interaction as a way to investigate shock propagation in an opaque solid. This is exemplified by the emission of a 15-MHz planar US elastic wave used as a probe to monitor a nanosecond laser-driven shock wave of 0.65 GPa amplitude in a thick aluminum sample. The detection mechanism is based on the interaction of the probe wave and the shock. Varying the time delay $\Delta t$ between the respective emission times allows one to reconstruct the shock propagation. Such an elastic-based shock detection scheme could complete optical-based detection and bring a new perspective to the use of laser-driven shock waves.

We first introduce some physical basis related to interactions between shock and elastic plane waves. Second, one-dimensional hydrodynamic numerical simulations are used to quantify laser-induced surface loading and the corresponding acoustic impedance

*mathieu.ducousso@safrangroup.com

 

variation due to the induced shock wave [24]. Third, experimental investigations are presented for an aluminum plate. The detection mechanism, driven by elastic scattering detection, is not straightforward and is interpreted using a three-dimensional elastic simulation code [25]. Similar experiments involving titanium and water are presented in the Supplemental Material [26]. Finally, conclusions emphasize perspectives for the near future.

## II. SHOCK AND ELASTIC PLANE WAVES NONLINEAR INTERACTION

Shock wave formation and propagation are irreversible processes. Therefore, the problem cannot be treated simply using an acoustical point of view, which is intrinsically limited to adiabatic phenomena. Equations of continuity of mass, movement, and entropy must be considered, along with Rankine-Hugoniot (RH) jump relations through shocks. Their resolution gives rise to at least three notable points. First, an acoustic plane wave cannot reflect on the shock front, as the shock propagates at a velocity $c_s$ larger than the longitudinal speed of sound, $c_a$. A shock front perturbation, viewed by Brillouin as an "accompanying wave," is also attached to the shock front [17]. Second, the interaction gives rise to an entropy mode, convected by the upstream flow behind the shock. It must be considered to properly satisfy RH energy balance on the shock [16], but is of negligibly small amplitude in the case of a weak shock, as entropy jump is then of third order only. In the case of oblique incidence (not considered here) a vorticity mode has also to be taken into account. Third, the transmission coefficient of the acoustic wave on the shock depends on several parameters, notably the Mach number and the nonlinear parameters of the materials. Thus, the amplitude of the scattered wave may be greater than the amplitude of the incident wave [18].

The laser-driven shock wave profile is quantified using ESTHER software, a one-dimensional hydrodynamic code simulating surface sublimation due to laser-matter interaction. The resulting expanding dense plasma from the surface and, by reaction, the shock wave generation and propagation are solved by the resolution of the mechanical balance equations. The Mie-Grüneisen equation of state is used to account for nonlinear elasticity [24].

The simulations are performed according to the experimental conditions. The calculated surface loading is presented in Fig. 1(a). Lateral dimensions ($20 \times 20$ cm$^2$) are such that they can be considered infinite in lateral directions. The maximum pressure is around 0.65 GPa with a duration of around 10 ns at full width at half maximum (FWHM). Such dynamical loading is at the fringe of the aluminum Hugoniot elastic limit (HEL), also estimated at 0.65 GPa in laser-driven loading [25]. An illustration of the calculated relative variations of the density and of the acoustic velocity is presented in Fig. 1(b), at two times after laser illumination. At 300 ns, the shock has traveled around 1.6 mm, less than the sample thickness, and is a compressive shock wave. At 450 ns however, the shock has reflected on the back face, converting into an expansion or release wave. The nonlinear Mie-Grüneisen equation of state makes the velocity variation strongly dependent on the compressive (+0.3%) or release (−0.02%) nature of the shock, contrarily to the density variation (±0.5%). After 12 mm of propagation, the Mach number of the shock wave is around 0.002, with a rise time evaluated at 4 ns and a FWHM at 16 ns [26].

## III. EXPERIMENTS

Figure 2(a) presents the experimental setup. Shock waves are generated using 532-nm-wavelength laser pulses of 7 ns, with energy ranging from 1 to 6 J. Fluencies up to 8 GW/cm$^2$ can easily be reached. A diffractive optical element focuses the laser at the sample surface with an almost perfect circular top-hat profile of 3 mm in diameter with 4.5-GW/cm$^2$ laser fluency (unless specified otherwise) [25]. In the near field, the resulting laser-driven

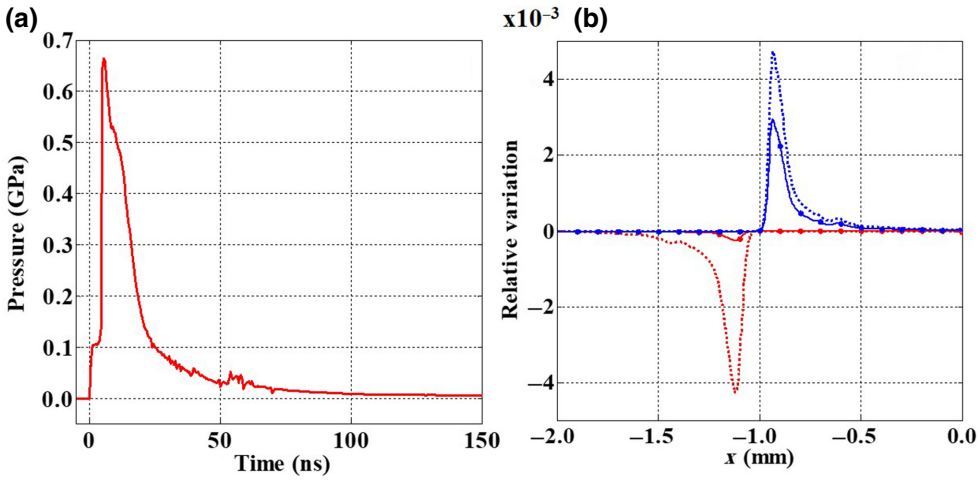


FIG. 1. (a) Surface pressure induced by a nanosecond laser pulse in aluminum. (b) Simulations of the density (dashed lines) and velocity (symbols) relative variations in a 2-mm-thick plate, 300 ns (blue) and 450 ns (red) after generation.

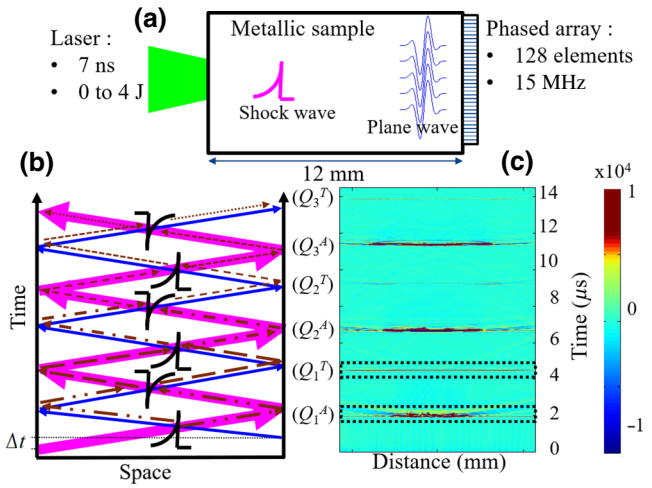


FIG. 2. (a) Principles of experiments. (b) Space-time representation: shock (plane wave) propagation is represented by the purple (blue) arrows and diffracted signals by dashed arrows. (c) Time-space PA detection of the pressure field. The dotted rectangles illustrate the temporal integration on the acoustic echoes for the investigation procedure.

shock wave has a similar circular flat profile with sharp edges. Diffraction at these edges additionally generates shear waves of significant amplitude [25], which are not considered in our work as they arrive much later than the main shock. Compared to simulation, a thick sample (12 mm in thickness) is used for the experiments, other parameters being identical. A phased array (PA) is coupled by an acoustic coupling gel to the back face of the sample [27], opposite to the laser focus. It contains 128 linearly aligned piezoelectric elements of $0.15 \times 5$ mm$^2$ elementary dimensions with a flat surface. The central acoustic frequency is 15 MHz. The PA is used in both emission and reception modes. In emission, the US probe wave of lateral dimensions around $23 \times 5$ mm$^2$ is counter-propagative with respect to the shock. The PA driver is locked onto the laser source with a time-delay driver. It allows one to adjust a time delay $\Delta t$ of several microseconds, with picosecond accuracy, between laser and US emission, changing the crossing point of the two waves inside the material [28]. Unless specified otherwise, $\Delta t = 0$. The PA driving voltage is raised to its maximum value (100 V) to emit a wave as intense as possible. The stress field is estimated (by the manufacturer) at 3 MPa inside the sample, 216 times smaller than the shock amplitude. A minimum analogic gain of the PA driver is used (5 dB) in order to unsaturate the detected signal from the shock wave.

The performance analysis of the experimental setup is quantified over 30 identical sequences of generation-detection of US and shock waves. The reproducibility of the PA generation-detection is evaluated for each element of the PA with a measured standard deviation of $10^{-3}$. The reproducibility of the shock generation-PA detection is similarly measured, with a standard deviation of around $10^{-2}$. The difference can be explained mainly by shot-to-shot fluctuations of the laser intensity, which can be increased by the nonlinear optical processes of shock generation [24]. The accuracy of the overall experimental setup is therefore of the same order of magnitude as the relative impedance variation induced by the shock wave (around $\pm 0.7\%$). The relative amplitude of the detected signal being around 0.1 (see later), the measured signal is one order of magnitude larger than the noise level of the detection. This relatively large value will now be shown to allow a monitoring of the shock propagation process. An alternative is to use the Doppler frequency shift resulting from the interaction between the counter-propagating probe wave and moving shock. It is quantified at around 0.3 MHz for each round trip in the structure. However, this shift is too small with respect to the complex frequency spectrum of the probe and cannot be clearly outlined experimentally [26].

## IV. RESULTS AND DISCUSSION

A time-space representation of the involved waves, Fig. 2(b), is used to infer the experimental strategy for the proposed shock elastography. The measured intensity field is $u_i^m(x) = \int p_i^2(x,t)dt$, with $p_i$ the pressure field detected at a PA element (position $x$) for each $i$th back-and-forth travel [see Fig. 2(c)]. It can be decomposed into two contributions, a reference signal (denoted $r$) and a scattered one (denoted $s$): $u^m = u^r + u^s$. We define the relative variation ratio $Q_i = {u_i}^m/{u_i}^r = 1 + {u_i}^s/{u_i}^r$, with superscript $T$ ($A$) when measuring the arrival of the transmitted probe pulse (when measuring the arrival of the shock pulse and its perturbation). This is possible because probe and shock arrivals are well separated in time. In the experiments, $u^m = u^r + u^s$ is detected at the PA when both plane and shock waves are generated and detected. The reference ${u_i}^r$ for ${Q_i}^T$ (${Q_i}^A$) evaluation is measured when emitting only the probe (shock).

The ratios ${Q_1}^A$ and ${Q_1}^T$ are presented in Figs. 3(a) and 3(b), respectively, over 10 different, but identical, experimental acquisitions (blue dotted lines). Their mean values are also presented as the red thick lines. This averaging allows increasing the SNR. Detection of ${Q_1}^T$ is strongly reproducible while more variations appear for ${Q_1}^A$. This could be attributed to the particular nature of ${Q_1}^A$ (i.e., a shock perturbation, and not a reflected wave) and to waves superposed in the detection: probe for $Q^T$ versus shock for $Q^A$. Both curves have a symmetric shape, centered on laser axis. The ${Q_1}^A$ curves feature two negative and symmetric peaks, while ${Q_1}^T$ presents a V shape with a clear central dip (10%). This amplitude is unexpectedly large. This could be related to the

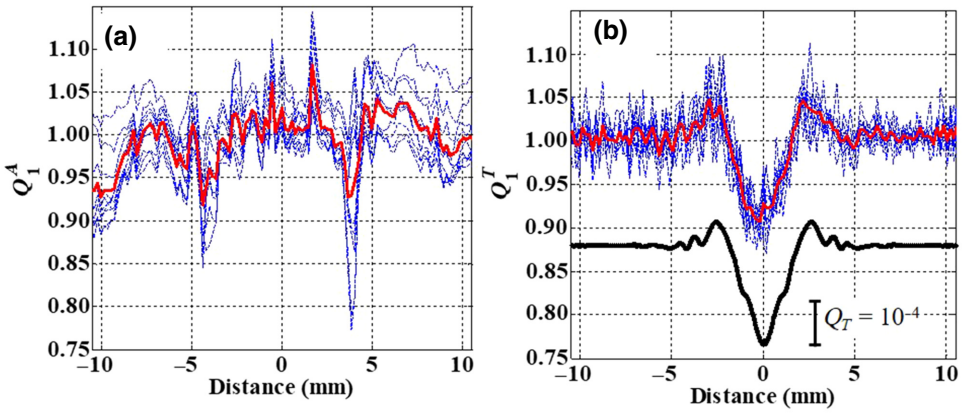


FIG. 3. Detection of ratio $Q_1{}^A$ (a) and $Q_1{}^T$ (b) from single-shot detection (blue dotted lines) and averaging of 10 detections (red continuous line). In (b), the signal presented in black (with its own amplitude scale) is obtained from linear simulations of a static inclusion.

supersonic motion of the shock discontinuity. A correct description should generalize the nonlinear approach of Burgers, Brillouin, and McKenzie and Westphal. However, their simplified assumption of a static step shock has to be abandoned. Moreover, the nonuniformity of the flow behind it should be considered. Indeed, a 100-ns shock duration (Fig. 1), comparable to the US probe period (66 ns at 15 MHz), may ensure a maximum interaction.

A preliminary model uses an elastic wave approach [25], replacing the shock by a 3-mm-diameter inclusion with density and sound speed values provided by ESTHER [Fig. 1(b)]. The resulting scattering profile [Fig. 3(b)] ideally reproduces the experimental V shape, including the strongly attenuated lateral oscillations likely due to the Fresnel diffraction of the probe on the shock circumference [29]. However, a huge difference (three decades) in amplitude remains. As already outlined, this is attributed

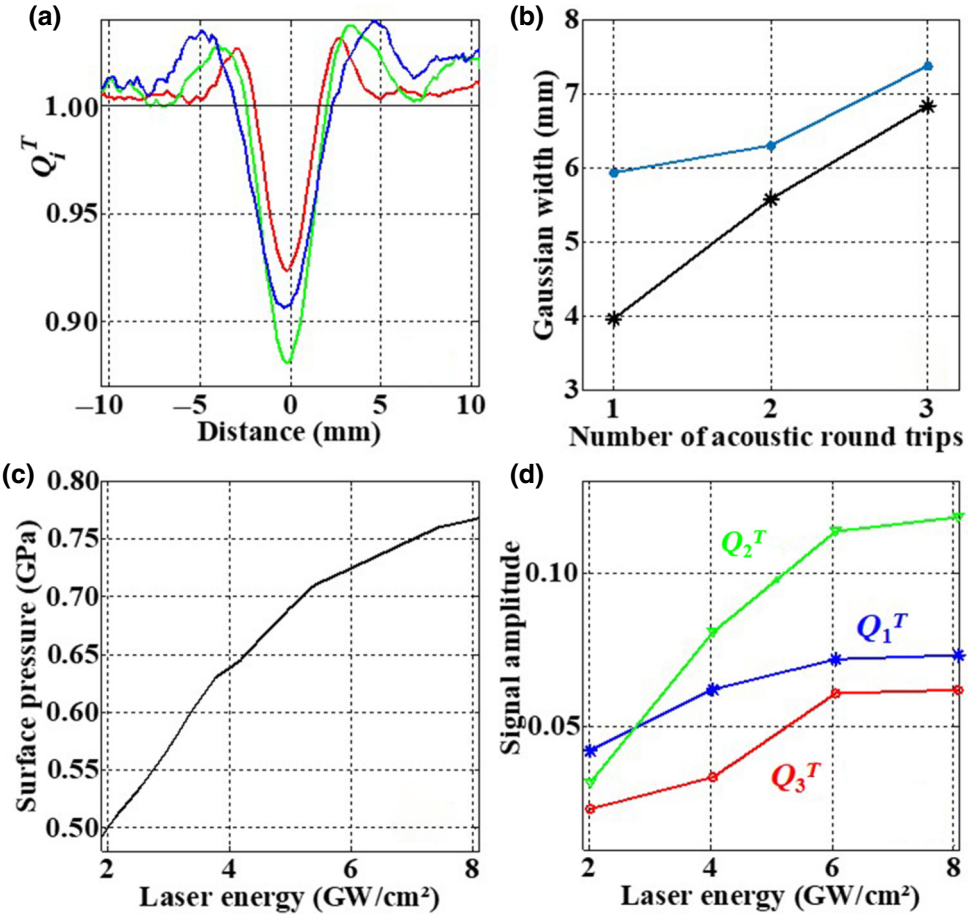


FIG. 4. (a) Average detection of $Q_i{}^T$ [$i = 1$ (red), 2 (green), 3 (blue)]. (b) FWHM of $Q_i{}^T$ for a laser focus of 3 mm (black stars) and 5 mm (blue points) in diameter. (c) Laser pressure loadings as function of the laser intensity from ESTHER simulations. (d) Intensity of the detected signal $Q_i{}^T$, $i = 1$ to 3, as a function of the laser intensity.

to the oversimplified linear acoustic model. Anyway, it can be attributed only to the interaction with the longitudinal shock wave as this characteristic shape is also observed in water [26].

Figure 4(a) presents $Q_i^T$ for up to three round trips in the material. One observes a widening with the number of acoustic trips, linked to the broadening of the shock beam along its propagation and to the directivity of the probe scattering on the shock edge. Figure 4(b) compares the spatial width of $Q_i^T$, $i=1$ to 3, for a 3-mm (asterisks) and a 5-mm (dots) laser diameter (denoted $D$). The observed increase is almost linear with respect to the number of round trips for $D=3$ mm. For $D=5$ mm, the size is nearly constant during the first two acoustic travels and shows beyond a growth similar to the previous case. Considering the PA frequency, Rayleigh distance $Z=D^2/2\lambda$, where $\lambda$ is the acoustic wavelength, is close to 17 (48) mm with a laser diameter of 3 (5) mm. Therefore, in the $D=3$ mm case, the successive detections are all performed in the diverging far-field regime, while in the second case the near-to-far-field transition occurs during the second round trip, explaining the observed widening. This close link between detection, laser spot diameter, and longitudinal shock broadening confirms that the process is only due to the probe-shock interaction.

Signals $Q_i^T$, $i=1$ to 3, for laser energies from 2 to 8 GW/cm$^2$ are reported in Fig. 4(d) and compared to surface pressures simulated using ESTHER, Fig. 4(c), increasing continuously with the laser intensity up to 0.75 GPa, above the material HEL (0.65 GPa). This means that plastic and elastic deformations simultaneously arise for highest energies. However, plastic deformation is confined to the very first micrometer under the surface while elastic deformations can propagate over several millimeters [25]. Here, only the elastic deformation is probed at the center of the sample ($\Delta t=0$), which explains the observed plateau. We also note that $Q_i^T$ presents a nonmonotonic variation: $Q_3^T < Q_1^T < Q_2^T$ (also observed for $Q_i^A$ [26]). This probably results from a balance between the attenuation of the different waves and the cumulative scattering detection each time the probe wave is transmitted through the shock (twice per round trip).

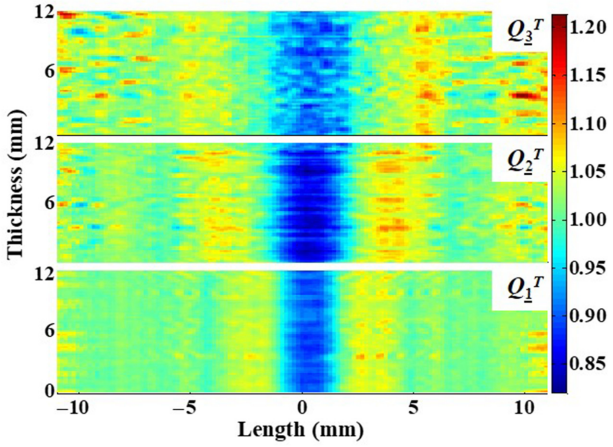


FIG. 5. Elastography of shock wave propagation during three round trips in the material.

Finally, introducing a time delay between shock and probe emissions allows tuning of the crossing point between them inside the bulk of the material and therefore allows monitoring of the shock propagation. Figure 5 shows a first experimental implementation. The ratios $Q_i^T$, $i=1$ to 3, are plotted as a function of space (horizontal axis) and depth (vertical axis). The shock widening is clearly imaged. The shock wave front is here planar, but a more complex one, related for instance to phase-induced transformations in materials or shock focalization (caustics), could be investigated.

## V. CONCLUSION

To conclude, we have designed an efficient way to monitor longitudinal shock wave propagation using an US probe. The method relies on the detection of the probe transmission through the shock. We assume that the observed high amplitude of the phenomenon results from a singular interaction between acoustic and shock waves, predicted in the middle of the twentieth century but not observed in solids. A numerical model is currently under development to confirm this. The Doppler effect could also be used as a complementary approach to quantify bulk shock properties. A broad range of applications could be explored using PA versatility, which allows the generation of plane waves of different angles with respect to the shock direction, or focusing probes for instance [27].

This time-space acoustic monitoring of shock propagation is intrinsically complementary to optics-based detection, from the visible to the X-ray range. It could bring new understandings to numerous domains, from the physics of weak shocks (here considered) to warm dense matter investigations, including laser-driven shock waves used to simulate accretion or giant and high-velocity impacts of astrophysical bodies and that are currently imaged using X-FEL facilities only. Other applications include the study of caustics in wave physics or laser-matter interaction and surface strain generation, which could be investigated using surface plane waves [30]. Laser ultrasonics could also be used as a probe instead of a PA to reach picosecond time resolution [31].

[1] Y. M. Gupta, S. J. Turneaure, K. Perkins, K. Zimmerman, N. Arganbright, G. Shen, and P. Chow, Real-time, high-resolution X-ray diffraction measurements on shocked

crystals at a synchrotron facility, Rev. Sci. Instrum. **83**, 123905 (2012).

[2] A. Schropp, R. Hoppe, V. Meier, J. Patommel, F. Seiboth, Y. Ping, D. G. Hicks, M. A. Beckwith, G. W. Collins, A. Higginbotham *et al.*, Imaging shock waves in diamond with both high temporal and spatial resolution at an XFEL, Sci. Rep. **5**, 11089 (2015).

[3] J. Ophir, I. Céspedes, H. Ponnekanti, Y. Yazdi, and X. Li, Elastography: A quantitative method for imaging the elasticity of biological tissues, Ultrason. Imaging **13**, 111 (1991).

[4] K. J. Parker, M. M. Doyley, and D. J. Rubens, Imaging the elastic properties of tissue: The 20 year perspective, Phys. Med. Biol. **5**, 5359 (2012).

[5] G. Pinton, J. Gennisson, M. Tanter, and F. Coulouvrat, Adaptive motion estimation of shear shock waves in soft solids and tissue with ultrasound, IEEE Trans. Ultrason. Eng. **61**, 1489 (2014).

[6] Y. Mariappan, K. J. Glaser, and R. L. Ehman, Magnetic resonance elastography: A review, Clin. Anat. **23**, 497 (2010).

[7] S. Catheline, J.-L. Gennisson, M. Tanter, and M. Fink, Observation of Shock Transverse Waves in Elastic Media, Phys. Rev. Lett. **91**, 164301 (2003).

[8] D. Espíndola, S. Lee, and G. Pinton, Shear shock waves observed in the brain, Phys. Rev. A **8**, 044024 (2017).

[9] J.-L. Gennisson, T. Deffieux, M. Fink, and M. Tanter, Ultrasound elastography: Principles and techniques, Diagn. Interv. Imaging **94**, 487 (2013).

[10] A. Itoh, E. Ueno, E. Tohno, H. Kamma, H. Takahashi, T. Shiina, M. Yamakawa, and T. Matsumura, Breast disease: Clinical application of US elastography for diagnosis, Radiology **239**, 341 (2006).

[11] L. M. Barker and R. E. Hollenbach, Laser interferometer for measuring high velocities of any reflecting surface, J. Appl. Phys. **43**, 4669 (1972).

[12] E. Ageev, S. Kudryashov, N. Nikonorov, R. Nuryev, A. Petrov, A. Samokhvalov, and V. Veiko, Non-contact ultrasonic acquisition of femtosecond laser-driven ablative mbar-level shock waves on Ti alloy surface, Appl. Phys. Lett. **108**, 084106 (2016).

[13] A. Denoeud, N. Ozaki, A. Benuzzi-Mounaix *et al.*, Dynamic X-ray diffraction observation of shocked solid, Proc. Natl. Acad. Sci. **113**, 7745 (2016).

[14] M. Ducousso, S. Bardy, Y. Rouchausse, T. Bergara, F. Jenson, L. Berthe, L. Videau, and N. Cuvillier, Quantitative evaluation of the mechanical strength of titanium/composite bonding using laser-generated shock waves, Appl. Phys. Lett. **112**, 111904 (2018).

[15] J. Wu, J. Zhao, H. Qiao, X. Hu, and Y. Yang, The new technologies developed from laser shock processing, Materials **13**, 1453 (2020).

[16] J. M. Burgers, On the transmission of sound waves through a shock wave, *Koninklijke Nederlandse Akademie van Wetenschappen*, Proc. XLIX, 273–281 (1946) (reproduced in *Selected Papers of J.M. Burger*s, Springer, pp. 478–486, 1995).

[17] L. Brillouin, Reflexion et refraction d'ondes acoustiques par une onde de choc, Acoustica **5**, 149 (1955).

[18] J. F. McKenzie and K. O. Westphal, Interaction of linear waves with oblique shock waves, Phys. Fluids **11**, 2350 (1968).

[19] J. C. Robinet, J. Gressier, G. Casalis, and J. M. Moschetta, Shock wave instability and the carbuncle phenomenon: Same intrinsic origin?, J. Fluid Mech. **4**, 237 (2000).

[20] K. Mahesh and S. Lee, The interaction of an isotropic field of acoustic waves with a shock wave, J. Fluid Mech. **300**, 383 (1995).

[21] J. R. Spreiter, A. Y. Alksne, and A. L. Summers, *Physics of the Magnetosphere* (Springer, Dordrecht, 1968), p. 301.

[22] W. I. Axford, *Acceleration of Cosmic Rays by Shock Waves* (Springer, Berlin, Heidelberg, 1969).

[23] A. Morro, Interaction of acoustic waves with shock waves in elastic solids, Z. Angew. Math. Phys. **29**, 822 (1978).

[24] S. Bardy, B. Aubert, T. Bergara, L. Berthe, O. Combis, D. Hébert, E. Lescoute, Y. Rouchausse, and L. Videau, Development of a numerical code for laser-induced shock waves applications, Opt. Laser Technol. **124**, 105983 (2020).

[25] E. Cuenca, M. Ducousso, A. Rondepierre, L. Videau, N. Cuvillier, L. Berthe, and F. Coulouvrat, Propagation of laser-generated shock waves in metals: 3D axisymmetric simulations compared to experiments, J. Appl. Phys. **128**, 244903 (2020).

[26] See Supplemental Material at http://link.aps.org/supplemental/10.1103/PhysRevApplied.15.L051002 for shock wave parameter evaluation, results for accompanying wave, results obtained in titanium and water, and Doppler effect analysis.

[27] B. W. Drinkwater and P. D. Wilcox, Ultrasonic arrays for non-destructive evaluation: A review, NDT&E Int. **39**, 525 (2006).

[28] M. Ghrib, L. Berthe, N. Mechbal, M. Rébillat, M. Guskov, R. Ecault, and N. Bedreddine, Generation of controlled delaminations in composites using symmetrical laser shock configuration, Compos. Struct. **171**, 286 (2017).

[29] F. Coulouvrat and R. Marchiano, Nonlinear fresnel diffraction of weak shock waves, J. Acoust. Soc. Am. **114**, 1749 (2003).

[30] M. Ducousso and F. Reverdy, Real-time imaging of microcracks on metallic surface using total focusing method and plane wave imaging with Rayleigh waves, NDT&E Int. **116**, 102311 (2020).

[31] C. B. Scruby and L. E. Drain, *Laser Ultrasonics Technique & Applications* (Adam Hilger, Bristol, 1990).